
Article:
Thoroughgood, T.D., Dhillon, V.S. orcid.org/0000-0003-4236-9642, Steeghs, D. et al. (7 more authors) (2005) The component masses of the cataclysmic variable V347 Puppis. Monthly Notices of the Royal Astronomical Society, 357 (3). pp. 881-894. ISSN 0035-8711

https://doi.org/10.1111/j.1365-2966.2004.08613.x

Mon. Not. R. Astron. Soc. **357,** 881–894 (2005) doi:10.1111/j.1365-2966.2004.08613.x

The component masses of the cataclysmic variable V347 Puppis

T. D. Thoroughgood,[1⋆] V. S. Dhillon,[1] D. Steeghs,[2] C. A. Watson,[1] D. A. H. Buckley,[3] S. P. Littlefair,[4] D. A. Smith,[1,5] M. Still,[6]† K. J. van der Heyden[3] and B. Warner[7]

[1]*Department of Physics and Astronomy, University of Sheffield, Sheffield S3 7RH*
[2]*Harvard-Smithsonian Center for Astrophysics, 60 Garden Street, MS-67, Cambridge, MA 02138, USA*
[3]*South African Astronomical Observatory, PO Box 9, Observatory 7935, Cape Town, South Africa*
[4]*School of Physics, University of Exeter, Stocker Road, Exeter EX4 4QL*
[5]*Winchester College, College Street, Winchester SO23 9LX*
[6]*NASA /Goddard Space Flight Center, Code 662, Greenbelt, MD 20771, USA*
[7]*Department of Astronomy, University of Cape Town, Private Bag, Rondebosch 7700, South Africa*

Accepted 2004 November 5. Received 2004 September 17; in original form 2004 June 19

ABSTRACT

We present time-resolved spectroscopy and photometry of the double-lined eclipsing cataclysmic variable V347 Pup (=LB 1800). There is evidence of irradiation on the inner hemisphere of the secondary star, which we correct for using a model to give a secondary-star radial velocity of $K_{\rm R} = 198 \pm 5$ km s^{-1}. The rotational velocity of the secondary star in V347 Pup is found to be $v \sin i = 131 \pm 5$ km s^{-1} and the system inclination is $i = 84\overset{\circ}{.}0 \pm 2\overset{\circ}{.}3$. From these parameters we obtain masses of $M_1 = 0.63 \pm 0.04$ M$_\odot$ for the white dwarf primary and $M_2 = 0.52 \pm 0.06$ M$_\odot$ for the M0.5V secondary star, giving a mass ratio of $q = 0.83 \pm 0.05$. On the basis of the component masses, and the spectral type and radius of the secondary star in V347 Pup, we find tentative evidence for an evolved companion. V347 Pup shows many of the characteristics of the SW Sex stars, exhibiting single-peaked emission lines, high-velocity S-wave components and phase-offsets in the radial velocity curve. We find spiral arms in the accretion disc of V347 Pup and measure the disc radius to be close to the maximum allowed in a pressureless disc.

Key words: accretion, accretion discs – binaries: eclipsing – binaries: spectroscopic – stars: individual: V347 Pup – novae, cataclysmic variables.

1 INTRODUCTION

Cataclysmic variables (CVs) are close binary stars consisting of a red dwarf secondary transferring material on to a white dwarf primary via an accretion disc or magnetic accretion stream. V347 Pup is an example of a nova-like variable (NL), a class of CV with high mass transfer rates and no recorded nova or dwarf-nova type outbursts; see Warner (1995a) for a comprehensive review of CVs.

A knowledge of the masses of the component stars in CVs is fundamental to our understanding of the origin, evolution and behaviour of these systems. Population synthesis models (e.g. Kolb, King & Baraffe 2001) and the disrupted magnetic braking model of CV evolution (e.g. Rappaport, Verbunt & Joss 1983; Spruit & Ritter 1983) can be observationally tested only if the number of reliably known CV masses increases. One of the most reliable ways to measure the masses of CVs is to use the radial velocity and the rotational broadening of the secondary star in eclipsing systems. The radial velocity of the disc emission lines is often an unreliable indicator of the white dwarf motion because of contamination from, for example, the bright spot. At present, reliable masses are known for only ∼20 CVs, partly due to the difficulties in measurement (see Smith & Dhillon 1998, for a review).

V347 Pup was identified spectroscopically as a NL by Buckley et al. (1990) from the presence of high-excitation emission lines. Even though V347 Pup emits at X-ray wavelengths (as the *Uhuru* X-ray source 4U 0608–49), the NL classification was favoured over a magnetic CV class on account of the negligible polarization present. The study by Buckley et al. (1990) revealed a bright and deeply eclipsing system, with a spectroscopic and photometric orbital period of 5.57 h. Their measured system inclination and emission-line radial velocity curve, together with an empirical secondary-star mass estimated from the orbital period, suggested a high primary mass close to the Chandrasekhar limit.

A multiwavelength study by Mauche et al. (1994) revealed an X-ray spectral energy distribution similar to many dwarf novae in outburst, with a likely origin in an extended emission region rather than the boundary layer. The UV emission lines appear to have a similar origin and, in a later paper by Shlosman, Vitello & Mauche (1996), their behaviour in eclipse was successfully modelled as disc

⋆E-mail: Tim.Thoroughgood@shef.ac.uk
†Also Universities Space Research Association.

light scattered in a rotating wind. The presence of an accretion disc in V347 Pup was confirmed by a rotational disturbance of the optical emission lines through primary eclipse (Mauche et al. 1994; Still, Buckley & Garlick 1998). The latter authors found evidence for spiral arms and disc overflow accretion, and identified the low-excitation optical emission profiles as a composite of emission from the accretion disc and secondary star.

Secondary-star absorption lines were found by Diaz & Hubeny (1999), who measured the system parameters of V347 Pup using the radial velocity semi-amplitudes of the primary and secondary stars. The radial velocity of the optical emission lines in V347 Pup varies widely in the literature, with published values of 134 ± 9 km s^{-1} (Buckley et al. 1990), 122 ± 19 km s^{-1} (Mauche et al. 1994), 156 ± 10 km s^{-1}, 125 ± 13 km s^{-1} (Still et al. 1998) and 193 ± 16 km s^{-1} (Diaz & Hubeny 1999). The radial velocities of the UV emission lines published by Mauche et al. (1994) ranged between 220 and 370 km s^{-1} with large phase shifts between spectroscopic conjunction and photometric mid-eclipse. This wide range in values, and the known unreliability of using disc emission lines in NLs to determine the motion of the white dwarf (e.g. Dhillon, Marsh & Jones 1997), makes the determination of system parameters from the secondary-star features alone highly desirable. In this paper, we derive the system parameters from the radial and rotational velocities of the secondary star in V347 Pup.

2 OBSERVATIONS AND REDUCTION

During 1998 January and December and 1999 January, we obtained optical spectra of V347 Pup using the Cassegrain spectrograph + SITe1 CCD chip on the South African Astronomical Observatory (SAAO) 1.9-m telescope. Simultaneous photometry was available for most of the spectra using the SAAO 1.0-m telescope with the TEK8 CCD chip. See Table 1 and its caption for full details.

On the 1998 December run, we observed 17 spectral type templates ranging from G7V to M5.5V and telluric stars to remove atmospheric features. We observed flux standards on both the 1.9-m and 1.0-m telescopes on all nights.

The spectra and images were reduced using standard procedures (e.g. Dhillon, Jones & Marsh 1994; Thoroughgood et al. 2001). The photometry data were corrected for the effects of atmospheric extinction by subtracting the magnitude of a nearby comparison star. The absolute photometry is accurate to approximately ± 0.5 mJy; the relative photometry to ± 0.01 mag. Comparison arc spectra were taken every $\sim$40 min in order to calibrate the wavelength scale and instrumental flexure. The arcs were fitted with fourth-order polynomials with an rms scatter of better than 0.04 Å. Where possible, slit losses were then corrected for by multiplying each V347 Pup spectrum by the ratio of the flux in the spectrum (over the whole spectral range) to the corresponding photometric flux.

3 RESULTS

3.1 Ephemeris

The times of mid-eclipse for V347 Pup were determined by fitting a parabola to the eclipse minima in the photometry data. A least-squares fit to the 21 eclipse timings listed in Table 2 yields the ephemeris:

$$T_{\text{mid-eclipse}} = \text{HJD } 244\,6836.961\,76 + 0.231\,936\,060\,E \pm 0.000\,09 \pm 0.000\,000\,006 \quad (1)$$

Our new ephemeris is exactly the same as that given by Baptista & Cieslinski (1991), except we have reduced the errors on both the zero point and orbital period. We find no evidence for any systematic variation in the O–C values listed in Table 2.

3.2 Average spectrum

The average spectra of V347 Pup, uncorrected for orbital motion, are shown in Fig. 1. In Table 3, we list fluxes, equivalent widths (EWs) and velocity widths of the most prominent lines measured from the average spectra.

The Balmer emission lines are broad, symmetric and single-peaked, instead of the double-peaked profile one would expect from a high-inclination accretion disc (e.g. Horne & Marsh 1986). This behaviour is characteristic of the SW Sex stars (e.g. Dhillon et al. 1997). Previous studies of V347 Pup by Buckley et al. (1990) and Diaz & Hubeny (1999) agree with this single-peaked observation; however, the study by Still et al. (1998) shows double-peaked low-excitation lines (although this could be due to the presence of absorption cores). The He I λ6678 line appears to be composed of a narrow single-peaked component superimposed upon a broad double-peaked component. The other He I emission lines can clearly be seen in the wavelength region centred on λ4610 as double peaked in nature, with the possible exception of He I λ4471. High-excitation

Table 1. Journal of observations. During 1998 January, we used Grating No. 4 to give a wavelength range of $\sim$4200–5060 Å ($\lambda_{\text{cen}} = 4610$) at 0.99-Å (64 km s^{-1}) resolution. Grating No. 4 was again used on 1998 December 28 and 1999 January 23 to give a wavelength range of $\sim$4900–5720 Å ($\lambda_{\text{cen}} = 5290$) at 0.95-Å (54 km s^{-1}) resolution. On 1998 December 25 and 27, we used Grating No. 5 to give a wavelength range of $\sim$5960–6725 Å ($\lambda_{\text{cen}} = 6330$) at 0.88-Å (42 km s^{-1}) resolution. Simultaneous photometry for the 1998 December spectra was recorded in the Johnson–Cousins *V*- and *R*-bands. Photometry was also available during the 1998 January run in the Strömgren *b* and *y* filters. The seeing measured around 1.0 arcsec with photometric conditions on 1998 December 25 and 27 and 1999 January 23. On 1998 December 28, however, the seeing was poor and patchy high cloud was present. The seeing varied between 1.0 and 1.5 arcsec over the 1998 January run. The epochs are calculated using the new ephemeris presented in this paper (equation 1).

UT date	1.9-m λ_{cen} (Å)	No. of spectra	Exposure time (s)	Epoch start	Epoch end	1.0-m filter	No. of images	Exposure time (s)	Epoch start	Epoch end
1998 January 07	4610	113	200	17 178.62	17 179.91	*b*	843	30	17 178.88	17 179.93
1998 January 08	4610	32	200	17 182.88	17 183.23	*b*	105	30	17 183.83	17 184.04
1998 January 10	4610	117	200	17 191.94	17 192.94	*y*	1379	30	17 191.61	17 192.96
1998 January 11	4610	129	200	17 195.74	17 197.25	*b*	1217	30	17 195.81	17 197.08
1998 January 12	4610	116	200	17 200.09	17 201.44	*b*	373	30	17 200.14	17 200.52
1998 December 25	6330	68	300	18 696.47	18 697.55	*R*	962	30	18 696.32	18 697.65
1998 December 27	6330	61	300	18 705.18	18 706.17	*R*	748	30	18 704.95	18 706.25
1998 December 28	5290	23	300	18 709.63	18 710.16	*V*	442	30	18 709.50	18 710.29
1999 January 23	5290	64	300	18 821.30	18 822.49	no photometry available				

Table 2. Times of mid-eclipse for V347 Pup according to Buckley et al. (1990; B90), Baptista & Cieslinski (1991; BC91) and this paper.

Cycle (E)	HJD at mid-eclipse (2400 000+)	Uncertainty on HJD	O–C (s)	Reference
−4	46 836.0379	5×10^{-4}	335.96	B90
0	46 836.9621	5×10^{-4}	29.74	B90
39	46 846.0059	5×10^{-4}	−117.69	B90
43	46 846.9333	5×10^{-4}	−147.43	B90
48	46 848.0930	5×10^{-4}	−145.73	B90
56	46 849.9500	5×10^{-4}	−15.13	B90
65	46 852.0373	5×10^{-4}	−25.89	B90
69	46 852.9651	5×10^{-4}	−21.08	B90
78	46 855.0533	5×10^{-4}	45.92	B90
6177	48 269.631 36	1.5×10^{-4}	48.28	BC91
7583	48 595.733 25	1.1×10^{-4}	30.04	BC91
7587	48 596.660 22	9×10^{-5}	−36.85	BC91
17 179	50 821.391 99	5×10^{-4}	56.29	This paper
17 184	50 822.551 27	5×10^{-4}	21.70	This paper
17 192	50 824.406 76	5×10^{-4}	21.83	This paper
17 196	50 825.334 28	5×10^{-4}	2.46	This paper
17 197	50 825.566 11	5×10^{-4}	−6.70	This paper
18 697	51 173.470 35	1×10^{-4}	6.20	This paper
18 705	51 175.325 62	1×10^{-4}	−12.68	This paper
18 706	51 175.558 02	1×10^{-4}	26.54	This paper
18 710	51 176.485 19	1×10^{-4}	−22.21	This paper

emission is present through He I λ4686 and the C III/N III λλ4640–4650 Bowen fluorescence complex.

The secondary star is clearly visible in the average spectra as absorption lines of the neutral metals Ca I, Fe I and Mg I, as seen in Diaz & Hubeny (1999). Secondary-star features in the SW Sex stars are not unusual in the longer period systems, such as BT Mon (Smith, Dhillon & Marsh 1998), AC Cnc and V363 Aur (Thoroughgood et al. 2004).

3.3 Light curves

Fig. 2 shows the broad-band and emission-line light curves of V347 Pup. The emission-line light curves were produced by subtracting a polynomial fit to the continuum and summing the residual flux. All light curves are plotted as a function of phase following the ephemeris derived in Section 3.1.

The *b*-, *y*-, *V*- and *R*-band light curves show deep, asymmetrical primary eclipses with the egress lasting longer than ingress. Flickering is present in all light curves, as well as an increase in brightness approaching eclipse in the *b*-, *y*- and *V*-bands. The *b*- and *y*-band data recorded in 1998 January show no significant brightness variations during the run, with out-of-eclipse magnitudes of 13.3 ± 0.1 in both filters. The eclipse depths are 3.2 and 2.6 mag, respectively. We measure *R*-band out-of-eclipse magnitudes of 14.00 ± 0.05 mag on December 25, increasing in brightness to 13.45 ± 0.10 mag on December 27. The eclipse depth remains roughly the same at 2.1 mag and 2.0 mag, respectively. In the *V*-band, the out-of-eclipse magnitude is 14.10 ± 0.10 mag, with an eclipse depth of 2.6 mag. Photometric out-of-eclipse magnitudes in the literature range between 13.05 and 13.28 in *R*, and 13.2 and 13.58 in *V* (Buckley et al. 1990; Mauche et al. 1994), suggesting that our observations in 1998 December find V347 Pup around 0.5–1 mag fainter. Long-term variations in the magnitudes of NLs are not uncommon (e.g. Honeycutt 2001) and have been observed in other SW Sex stars (e.g. BH Lyn, Dhillon et al. 1992; DW UMa, Dhillon et al. 1994; PX And, Still, Dhillon & Jones 1995). Low states are often accompanied by the weakening or disappearance of the high-excitation He II and C III/N III lines, which were unfortunately not observed in 1998 December. There is, however, a change in the He I λ6678 Doppler maps between the observations on the two nights, which is considered in Section 3.4. Further evidence that V347 Pup exhibits changes of state is seen in the equivalent widths of the emission lines between the observed epochs. For example, the EW of Hβ varies between 17.0 ± 0.6 Å (1986 July, Buckley et al. 1990), 62.6 ± 1.9 Å (1991 April, Mauche et al. 1994), 9.8 ± 0.1 Å (1995 January,

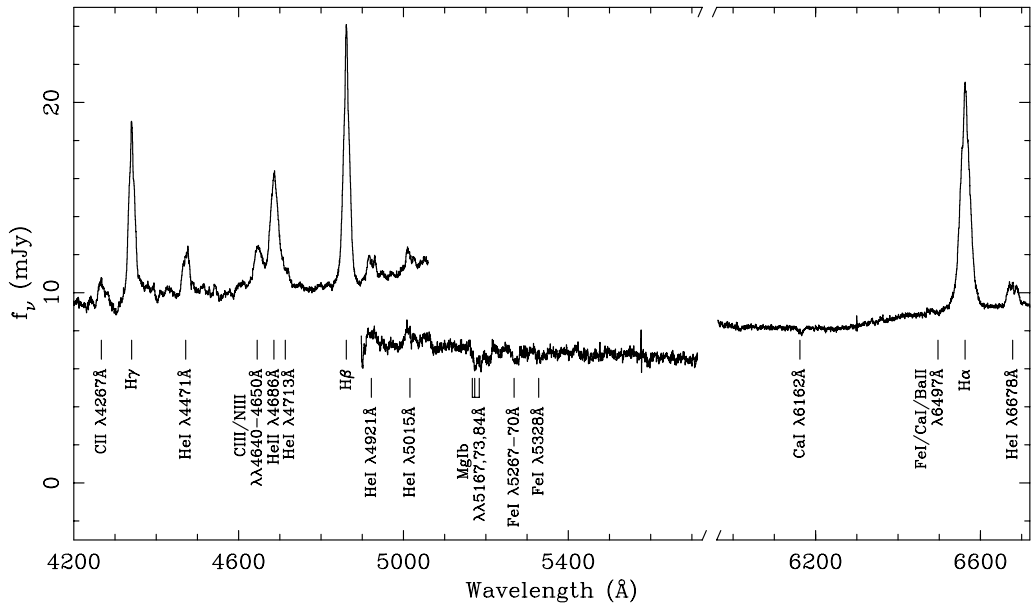

Figure 1. The average spectra for the three wavelength regions; the spectrum centred on λ4610 is an average of all spectra recorded on the 1998 January run, and has not been corrected for slit-losses. The spectrum centred on λ5290 is an average of all data recorded on 1998 December 28 and 1999 January 23, placed on an absolute flux scale (as determined from the 1998 December 28 photometry and flux standards). The spectrum centred on λ6330 is composed of all data from 1998 December 25 and 27 and has been placed on an absolute flux scale. All average spectra are uncorrected for orbital motion, resulting in smeared spectral features.

Table 3. Fluxes and widths of prominent lines in V347 Pup, measured from the data from the two nights centred on λ6330 Å and the night of 1998 January 11 centred on λ4610 Å. The full-width half-maximum (FWHM) velocities were determined from Gaussian fits, whereas the full-width zero-intensity (FWZI) velocities and their errors have been estimated by eye. He II λ4686, C III/N III λλ4640–4650 and He I λ4713 are blended, so separate values of the flux and EW are given (determined from a triple-Gaussian fit) as well as the combined flux of the three.

Line	Date	Flux ($\times 10^{-14}$ (ergs cm^{-2} s^{-1})	EW (Å)	FWHM (km s^{-1})	FWZI (km s^{-1})
Hα	1998 December 25	16.80 ± 0.04	35.1 ± 0.1	1100 ± 100	3500 ± 300
Hα	1998 December 27	27.98 ± 0.05	36.4 ± 0.1	1100 ± 100	3600 ± 300
Hβ	1998 January 11	42.2 ± 0.1	24.6 ± 0.2	1000 ± 100	2800 ± 300
Hγ	1998 January 11	34.6 ± 0.2	16.9 ± 0.3	1100 ± 100	2600 ± 800
He I λ4471	1998 January 11	8.0 ± 0.1	3.8 ± 0.2	1150 ± 100	1850 ± 200
He I λ4921	1998 January 11	4.23 ± 0.08	2.6 ± 0.1	1300 ± 100	2000 ± 200
He I λ5015	1998 January 11	3.3 ± 0.1	2.2 ± 0.2	1250 ± 100	2000 ± 200
He I λ6678	1998 December 25	1.49 ± 0.02	2.92 ± 0.08	1250 ± 100	1900 ± 200
He I λ6678	1998 December 27	2.40 ± 0.04	3.00 ± 0.08	1300 ± 100	1900 ± 200
C II λ4267	1998 January 11	3.8 ± 0.1	1.7 ± 0.4	900 ± 200	1800 ± 600
He II λ4686	1998 January 11	26.9 ± 0.3	13.1 ± 0.3	1450 ± 150	
C III/N III λλ4640–4650	1998 January 11	11.7 ± 0.1	6.4 ± 0.2	1700 ± 150	
He I λ4713	1998 January 11	4.8 ± 0.3	2.3 ± 0.3	1500 ± 300	
He II + C III/N III + He I λ4713	1998 January 11	45.5 ± 0.2	22.4 ± 0.2		

Still et al. 1998) and 24.6 ± 0.2 Å (1998 January, this paper), although the high-excitation C III/N III complex has a constant EW between epochs.

We measured the phase half-width of eclipse at the out-of-eclipse level ($\Delta\phi$) by timing the first and last contacts of the eclipse and dividing by 2. Our average value of $\Delta\phi = 0.110 \pm 0.005$ is consistent with the values of 0.120 ± 0.011 quoted by Harrop-Allin & Warner (1996) and 0.105 ± 0.005 measured by Buckley et al. (1990). We then computed the radius of the accretion disc in V347 Pup using the geometric method outlined in Dhillon, Marsh & Jones (1991). Combining $\Delta\phi$ with the system mass ratio and inclination derived in Section 3.10 gives an accretion disc radius ($R_{\rm D}$) of $0.72 \pm 0.09\,R_1$, where R_1 is the volume radius of the Roche lobe of the primary. This value is in agreement with the value of $R_{\rm D}/R_1 \geqslant 0.82$ quoted by Harrop-Allin & Warner (1996) at the 2σ level.

The Hα eclipses are similar in shape to the continuum light curves, but do not appear to be as deeply eclipsed. The Hβ and Hγ lines exhibit asymmetric eclipses, with ingress longer than egress. This behaviour is expected from asymmetric disc emission, consistent with the spiral arms identified in the Doppler maps (Section 3.4). The high-excitation He II + C III/N III complex has a deep and U-shaped eclipse, suggesting an origin close to the white dwarf. The He I eclipses are wide with V-shaped minima, similar to the SW Sex stars (e.g. Knigge et al. 2000). Note that the He I flux is completely eclipsed, indicating an origin in the central portion of the disc, and not in an extended emission region which is larger than the secondary star. The He I λ4471 emission line shows a broad dip in flux around phase 0.4, before climbing to reach a maximum around phase 0.75, which could be a further signature of the disc asymmetry.

3.4 Trailed spectrum and Doppler tomography

We subtracted polynomial fits to the continuum and then rebinned the spectra on to a constant velocity-interval scale centred on the rest wavelength of the principal emission lines. For the data obtained in 1998 January, we phase-binned all the spectra in order to boost the signal-to-noise ratio (S/N). Individual spectra were weighted according to their S/N in order to combine the spectra optimally. The trailed spectra of Hα, Hβ, He II λ4686 and He I λλ4471, 5015, 6678 are shown in Fig. 3. Doppler maps were calculated for the principal emission lines using the modulation Doppler tomography code of Steeghs (2003). This method is an extension to the conventional Doppler tomography technique (e.g. Marsh 2001), and maps both the constant and variable part of the line emission using a maximum-entropy regularized fitting procedure (Skilling & Bryan 1984). We found that the modulated contribution to the line emission was weak (<1 per cent), and thus our S/N was not sufficient to detect significant modulation in the accretion disc emission. We therefore plot in Fig. 4 the corresponding average Doppler maps only. The reconstructed line profiles are plotted next to the observed ones in Fig. 3 for comparison. Good fits to the data were achieved in all cases (reduced $\chi^2 = 1$–1.4)

The Balmer-line trailed spectra are dominated by a low-velocity component with a semi-amplitude of ∼150 km s^{-1}, moving from blue to red across primary eclipse. This is consistent with emission from the irradiated inner face of the secondary star, which is clearly seen in the corresponding Doppler maps. In the Hβ map, a second low-velocity emission source is present, seemingly coincident with the gas stream at a distance of $0.9L_1$, where L_1 is the distance from the white dwarf to the inner Lagrangian point. There is also a weak two-armed disc asymmetry visible in the Hβ emission, which is much more prominent in the double-peaked He I emission lines. Doppler maps of V347 Pup have been produced by Still et al. (1998) for data sets recorded in 1987, 1988 and 1995. The two components described above from the secondary star and the disc are clearly visible in their maps. The summed Hβ and Hγ maps of Still et al. (1998) show a stronger disc emission and spiral structure than our Balmer-line maps. The disc asymmetry is significant and is reminiscent of the two-armed spiral structures that have been observed in the discs of dwarf novae during outburst (e.g. Steeghs 2001). We return to these in Section 4.1. The high-excitation He II λ4686 line is dominated by emission from the gas stream and bright spot overlayed on a weak accretion disc with radius $R_{\rm D} \sim 0.3$–$0.4\,L_1$. Note that the He II λ4686 Doppler map shows emission at higher velocities than the low-excitation lines, demonstrating that the material originates from closer to the white dwarf.

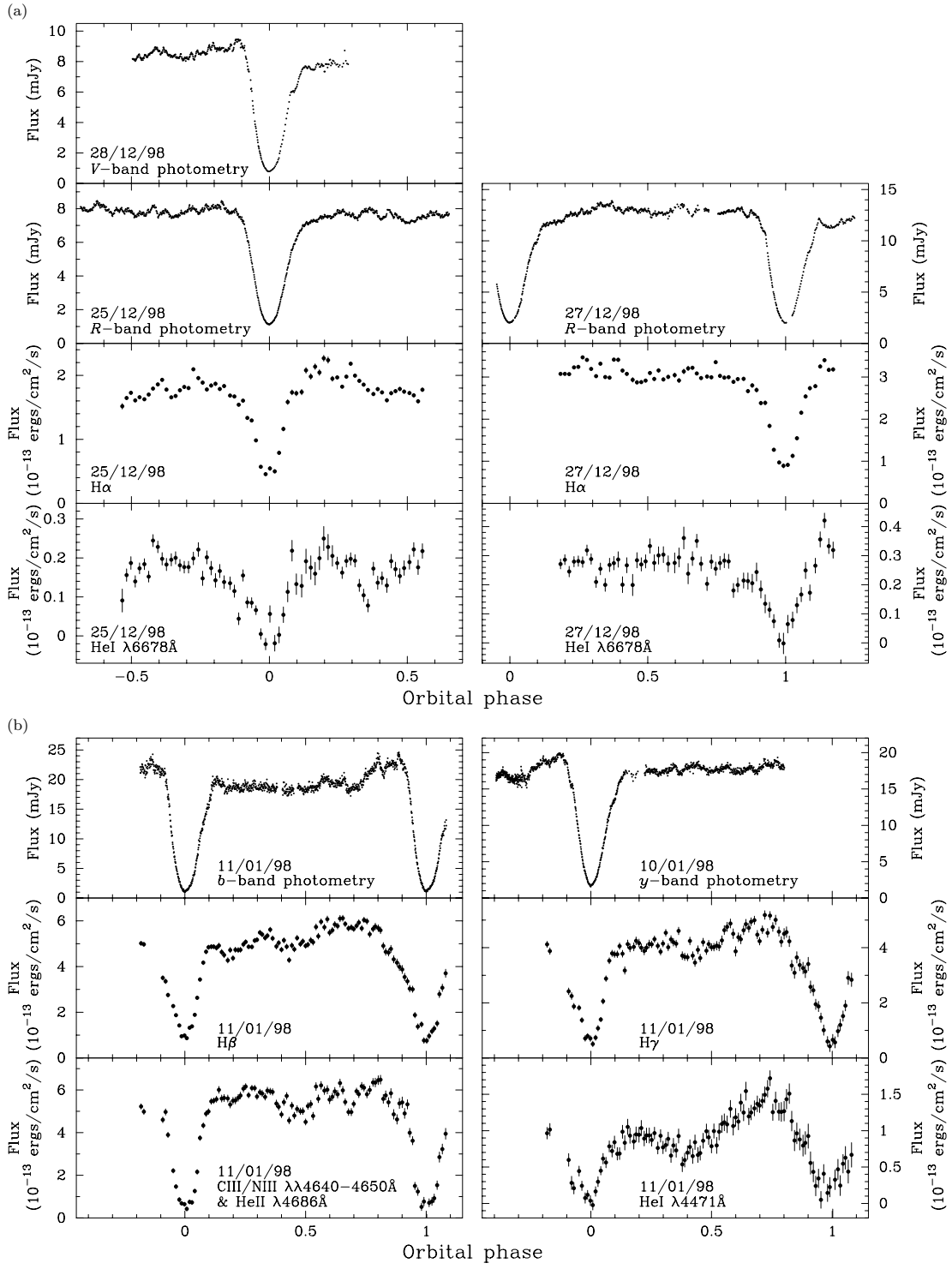

Figure 2. Broad-band and emission-line light curves of V347 Pup recorded in 1998 December and 1999 January (a), and 1998 January (b); see the panel labels for details. Note the increase in continuum and emission-line flux between 1998 December 25 and 27.

The blue and red He I emission lines were recorded almost a year apart and exhibit clear differences in structure. The secondary-star emission is clearly evident in He I λ6678 (1998 December), although no strong He I λ4471 or λ5015 emission can be seen in the 1998 January data. There is also a difference in the He I λ6678 Doppler maps between 1998 December 25 and 27, which is probably related to the change in brightness of the system; the 1998 December 25 Doppler map has more enhanced spiral features and weaker secondary-star emission than the December 27 (note that the average map of these two nights is shown in Fig. 4). During all these epochs, however, the spiral structures were observed, demonstrating that they are a persistent feature.

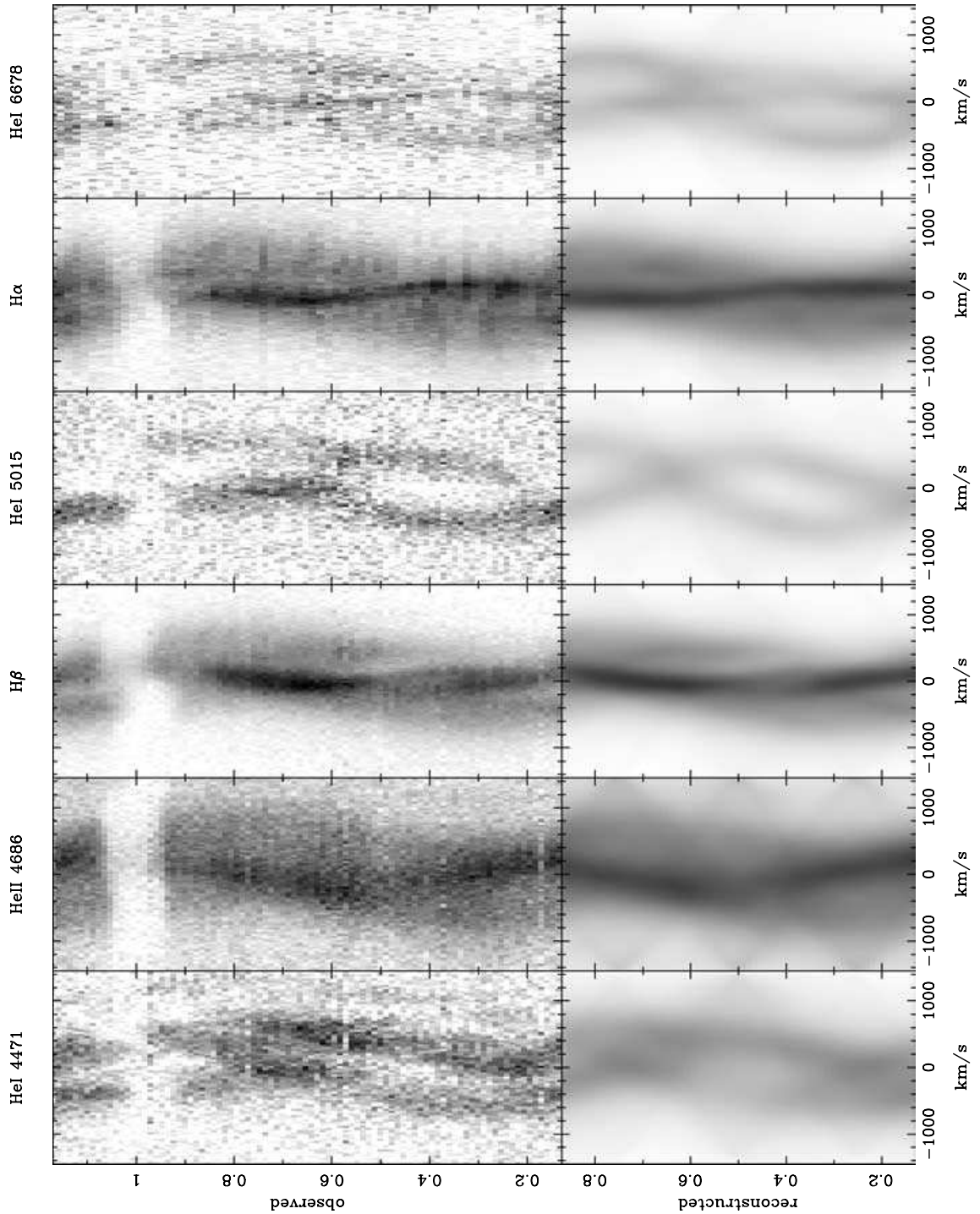

Figure 3. Trailed spectra and data computed from the Doppler maps (Fig. 4). The blue data recorded in 1998 January have been phase binned into 200-s bins, the red data recorded in 1998 December into 300-s bins. Hγ has not been shown, as it is very similar in nature to Hβ.

3.5 Radial velocity of the white dwarf

We measured the radial velocities of the emission lines in V347 Pup by applying the double-Gaussian method of Schneider & Young (1980), since this technique is sensitive mainly to the line wings and should therefore reflect the motion of the white dwarf with the highest reliability. We tried Gaussians of widths 200, 300 and 400 km s^{-1} and we varied their separation from 200 to 3200 km s^{-1}. We then fitted

$$V = \gamma - K \sin[2\pi(\phi - \phi_0)] \quad (2)$$

to each set of measurements, where V is the radial velocity, K the semi-amplitude, ϕ the orbital phase, and ϕ_0 is the phase at which the radial velocity curve crosses from red to blue. Examples of the radial velocity curves measured for the Hα, Hβ, He II λ4686 and He I λ4471 emission lines are shown in Fig. 5. There is clear

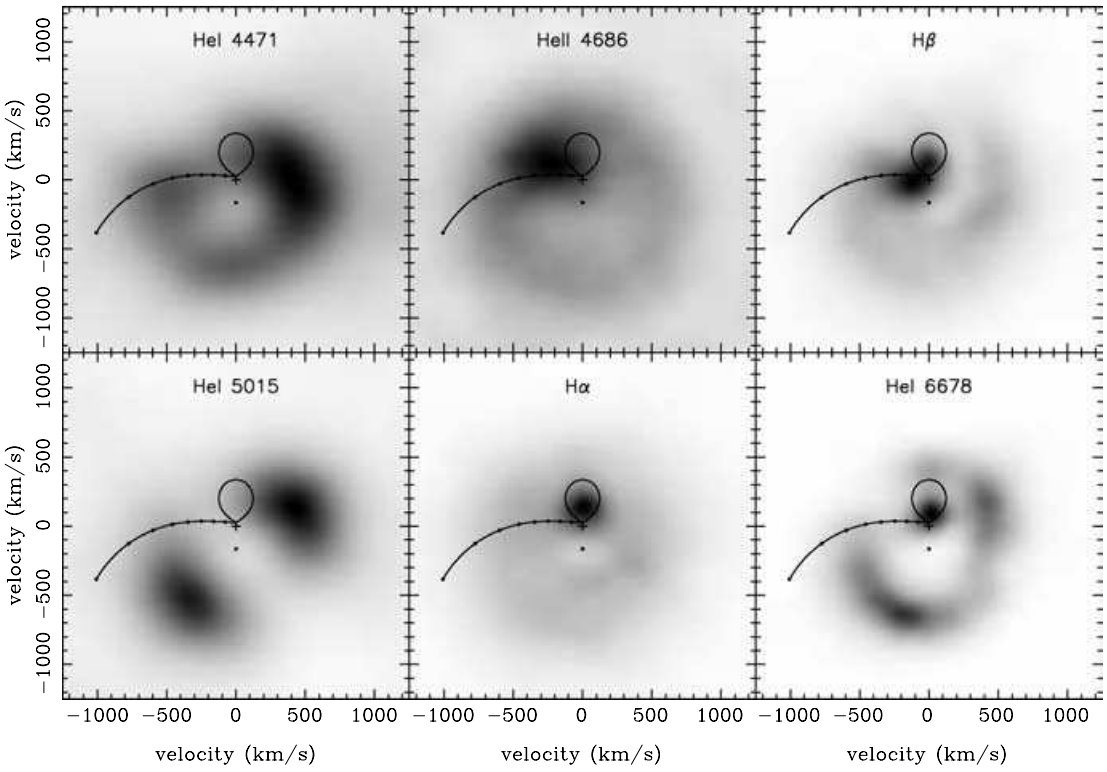

Figure 4. Doppler maps of the principal emission lines (Hγ is not shown, as it is very similar in nature to Hβ). The cross marked on each Doppler map represents the centre of mass of the system and the open circle represents the white dwarf. These symbols, the Roche lobe of the secondary star and the predicted trajectory of the gas stream, have been plotted using the $K_{\rm R}$-corrected system parameters summarized in Table 5. The series of points along the gas stream mark the distance from the white dwarf at intervals of $0.1L_1$, ranging from $1.0L_1$ at the red star to $0.2L_1$. Doppler tomography cannot properly account for variable line flux, so spectra around primary eclipse were omitted from the fits.

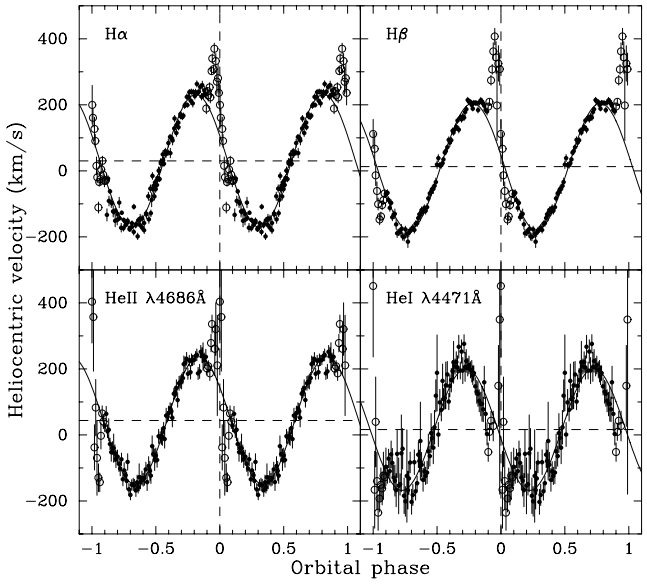

Figure 5. Radial velocity curves of Hα, Hβ, He II λ4686 and He I λ4471 using Gaussian widths of 300 km s^{-1} and a separation of 1400 km s^{-1}. We omitted the points around primary eclipse during the fitting procedure (open circles) as these measurements are affected by the rotational disturbance. The emission lines recorded in 1998 January have been phase-binned into 100 bins for clarity.

evidence of rotational disturbance in the emission lines, where the radial velocities measured just prior to eclipse are skewed to the red, and those measured after eclipse are skewed to the blue. This confirms the detection of a similar feature in the trailed spectra, and indicates that at least some of the emission must originate in the disc. There is also evidence of a phase shift in Hα and He II λ4686, where the spectroscopic conjunction of each line occurs after photometric mid-eclipse. This phase shift implies an emission-line source trailing the accretion disc, such as a bright spot, and is a common feature of SW Sex stars (e.g. DW UMa, Shafter, Hessman & Zhang 1988; V1315 Aql, Dhillon et al. 1991; SW Sex, Dhillon et al. 1997). There appear to be no significant phase shifts, however, in the other emission lines. Buckley et al. (1990), Mauche et al. (1994) and Diaz & Hubeny (1999) find no evidence of phase shift in any of their emission lines, although their errors on ϕ_0 were much larger.

We tried to measure white dwarf radial velocity ($K_{\rm W}$) values using a diagnostic diagram (Shafter, Szkody & Thorstensen 1986), but with no success. We therefore attempted to make use of the light-centres method, as described by Marsh (1988). In the corotating coordinate system, the white dwarf has velocity $(0, -K_{\rm W})$, and symmetric emission, say from a disc, would be centred at that point. By plotting $K_x = -K \sin\phi_0$ versus $K_y = -K \cos\phi_0$ for the different radial velocity fits (Fig. 6), one finds that the points move closer to the K_y axis with increasing Gaussian separation. A simple distortion which only affects low velocities, such as a bright spot, would result in this pattern, equivalent to a decrease in distortion as one measures emission further into the line wings and therefore more closely representing the velocity of the primary star. By linearly extrapolating

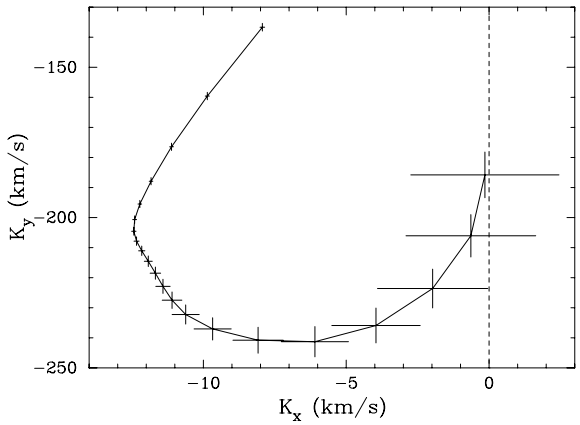

Figure 6. Light-centres diagram for Hα. Points are plotted for radial velocity fits using Gaussians of FWHM = 300 km s^{-1}, with separations from 900 km s^{-1} to 2900 km s^{-1} at 100 km s^{-1} intervals. The points move anticlockwise, towards the $K_x = 0$ axis with increasing Gaussian separation.

the largest Gaussian separation on the Hα light-centre diagram to the K_y axis, we measure the radial velocity semi-amplitude of the white dwarf to be $\sim$180 km s^{-1}. The large uncertainty in this value ($\sim$40 km s^{-1}), however, and the unsuccessful application of the technique to the other emission lines, prompted us to proceed with the mass determination using the secondary-star features alone.

3.6 Radial velocity of the secondary star

The secondary star in V347 Pup is clearly visible in Fig. 1 through absorption lines of Mg I, Fe I and Ca I. We compared regions of the spectra rich in absorption lines with a number of templates with spectral types G7V–M3.5V. A technique known as skew mapping was used to enhance the secondary features and obtain a measurement of the radial velocity semi-amplitude of the secondary star (K_R). See Vande Putte et al. (2003) for a detailed critique of skew mapping and Thoroughgood et al. (2004) for a successful application to AC Cnc and V363 Aur.

The data centred on λ5290 were recorded specifically to exploit the secondary-star features found between the Hβ and Hα lines. Unfortunately, the presence of weak emission lines (e.g. Fe II multiplet 42 at $\lambda\lambda$4924, 5018 and 5169, Mason & Howell 2003) hampered all efforts to determine a K_R value from these data. The dominance of the emission lines in the spectra centred on λ4610 also prevented a K_R determination from these data. The red spectra of V347 Pup centred on λ6330, however, allowed us to study the secondary star through absorption features blueward of Hα, such as the Ca I λ6162 line. Exactly the same conclusion was reached by Diaz & Hubeny (1999).

The first step was to shift the spectral type template stars to correct for their radial velocities. We then normalized each spectrum by dividing by a constant and then subtracting a polynomial fit to the continuum. This ensures that line strength is preserved along the spectrum. The V347 Pup spectra were normalized in the same way. The template spectra were artificially broadened to account for both the orbital smearing of the V347 Pup spectra due to their exposure times (t_{exp}), using the formula

$$V = \frac{t_{exp} 2\pi K_R}{P} \quad (3)$$

(e.g. Watson & Dhillon 2001), and the rotational velocity of the secondary ($v \sin i$). Estimated values of K_R and $v \sin i$ were used in the first instance, before iterating to find the best-fitting values given in Section 3.10. Regions of the spectrum devoid of emission lines were then cross-correlated with each of the templates, yielding a time series of cross-correlation functions (CCFs) for each template star. To produce the skew maps, these CCFs were then back-projected in the same way as time-resolved spectra in standard Doppler tomography (Marsh & Horne 1988). If there is a detectable secondary star, we expect a peak at (0,K_R) in the skew map. This can be repeated for each of the templates, and the final skew map is the one that gives the strongest peak.

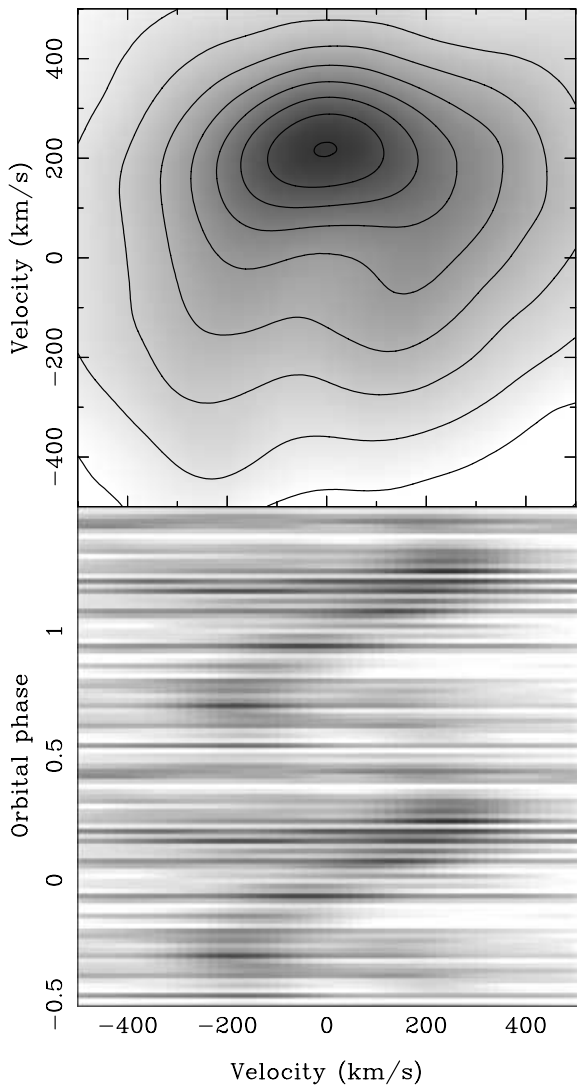

Figure 7. Skew maps (top) and trailed CCFs (bottom) of V347 Pup cross-correlated with a M0.5V dwarf template.

The skew maps show well-defined peaks at $K_y \approx 216$ km s^{-1} – the skew map of the M0.5V template is shown in Fig. 7 together with the trailed CCFs. A systemic velocity of $\gamma = 15$ km s^{-1} was applied in order to shift the skew map peaks on to the $K_x = 0$ axis (see Smith et al. 1998 for details). We therefore adopt $\gamma = 15 \pm 5$ km s^{-1} as the systemic velocity of V347 Pup, in excellent agreement with the values of 16 ± 10 km s^{-1} and 15 ± 12 km s^{-1} measured by Still et al. (1998) from the Balmer and He II λ4686 emission lines. The γ velocities from the emission lines shown in Fig. 5 ranged between 13 km s^{-1} and 44 km s^{-1}. Other γ values measured from optical

Table 4. $v \sin i$ values for V347 Pup cross-correlated with the rotationally broadened profiles of G7–M3.5V templates. Also shown is the factor used to multiply the template star features during optimal extraction, and the position of the strongest peak in the skew maps derived from each template using γ-velocities of 0 km s^{-1} and 15 km s^{-1}.

Templates	$v \sin i$ at min χ^2 (km s^{-1})	Optimal factor	(K_x, K_y) $\gamma = 0$ (km s^{-1})	(K_x, K_y) $\gamma = 15$ (km s^{-1})
G7V	134	0.32 ± 0.05	(−26,212)	(10,220)
G9V	133	0.28 ± 0.04	(−13,215)	(13,220)
K0V	133	0.23 ± 0.03	(−2,217)	(14,219)
K1V	134	0.24 ± 0.03	(−15,215)	(8,220)
K2V	133	0.20 ± 0.03	(−22,212)	(6,219)
K3V	136	0.19 ± 0.03	(−28,212)	(0,217)
K4V	135	0.14 ± 0.02	(−17,211)	(3,217)
K5V	134	0.13 ± 0.02	(−17,213)	(1,218)
K7V	133	0.12 ± 0.02	(−24,210)	(−3,216)
M0.5V	130	0.13 ± 0.02	(−18,213)	(0,216)
M1.5V	125	0.12 ± 0.02	(−17,213)	(−2,216)
M2.5V	126	0.13 ± 0.02	(−21,213)	(−7,216)
M3.5V	127	0.12 ± 0.02	(−33,213)	(−23,217)

emission lines vary widely in the literature (−3 to 60 km s^{-1}, Diaz & Hubeny 1999; –9 to 159 km s^{-1}, Mauche et al. 1994).

Our adopted K_R of 216 ± 5 km s^{-1} was derived from the skew map peak of the best-fitting template found in Section 3.10. This result actually covers the K_R values derived from *all* of the template stars to within the errors, demonstrating that the result is robust to the choice of template (see Table 4).

3.7 Rotational velocity and spectral type of the secondary star

The spectral-type templates were broadened for smearing due to orbital motion, as before, and rotationally broadened by a range of velocities (50–240 km s^{-1}). We then ran an optimal subtraction routine, which subtracts a constant times the normalized template spectrum from the normalized average V347 Pup spectrum, adjusting the constant to minimize the scatter in the residual. (Normalization was carried out in the same way as Section 3.6, except that this time, the spectra were set to unity.) The scatter is measured by carrying out the subtraction and then computing the χ^2 between the residual spectrum and a smoothed version of itself. By finding the value of rotational broadening that minimizes the χ^2, we obtain an estimate of both $v \sin i$ and the spectral type of the secondary star. Note that the $v \sin i$ values of the template stars are much lower than the instrumental resolution, so do not affect our measurements of $v \sin i$ for the secondary star.

The value of $v \sin i$ obtained using this method varies depending on the spectral type template, the wavelength region for optimal subtraction, the amount of smoothing of the residual spectrum in the calculation of χ^2 and the value of the limb-darkening coefficient used in the broadening procedure. The values of $v \sin i$ for all of the templates calculated using values for the limb-darkening coefficient of 0.5 and smoothed using a Gaussian of FWHM = 15 km s^{-1}, are listed in Table 4.

A plot of χ^2 versus $v \sin i$ for each spectral-type template is shown in Fig. 9. The spectral type with the lowest χ^2 value is M0.5V, which agrees with a visual identification of the best-fitting template. Diaz & Hubeny (1999), however, estimate a secondary-star spectral type between K0V and K5V, with the possibility of a later-type subgiant. A plot of the V347 Pup average spectrum, a broadened M0.5V template spectrum and the residual of the optimal subtraction is shown in Fig. 8. The χ^2 for the M0.5V template has a minimum at 130 km s^{-1}, so we adopt $v \sin i = 130 \pm 5$ km s^{-1}, with the error accounting for the measurement accuracy and the other variables noted in the previous paragraph. The error quoted on our adopted value encompasses the measured $v \sin i$ for all of the templates used in the analysis (except for K3V with $v \sin i = 136$ km s^{-1}).

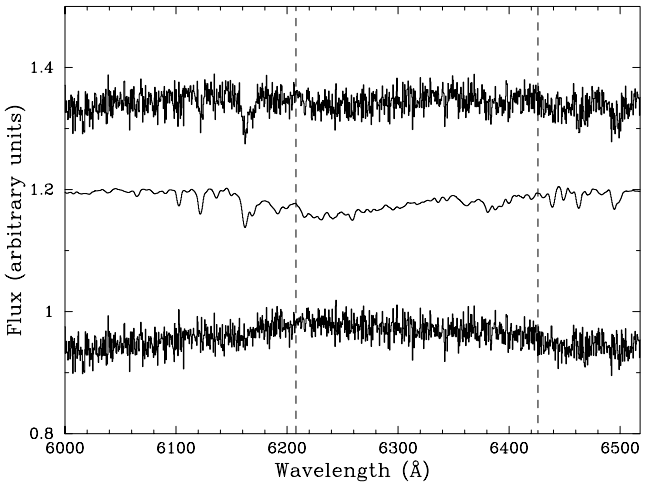

Figure 8. Orbitally corrected average spectrum of V347 Pup (top) with the broadened M0.5V template (middle) and the residuals after optimal subtraction (bottom). The template spectrum has been multiplied by the scaling factor found from the optimal subtraction. All of the spectra are normalized and offset on the plot by an arbitrary amount for clarity. The wavelength limits shown are those used for the cross-correlation and optimal subtraction procedures, except for the region between the dashed lines owing to few secondary-star features.

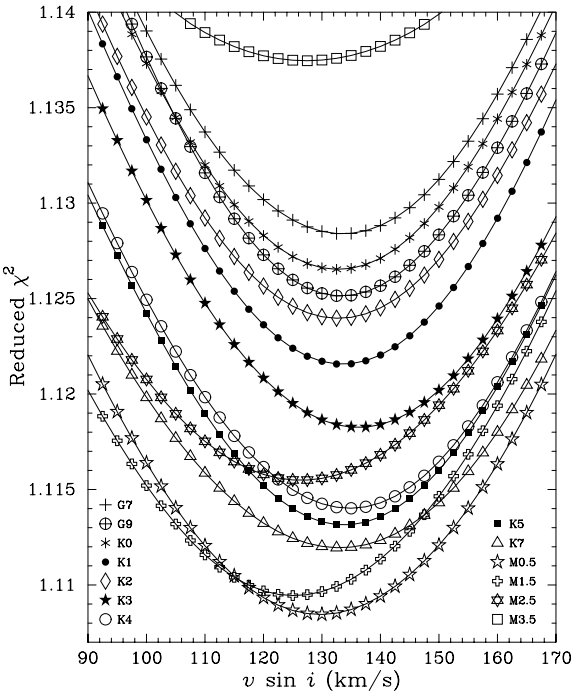

Figure 9. Determination of $v \sin i$ for V347 Pup using different spectral-type templates. Degrees of freedom = 699.

3.8 The K_R correction

The irradiation of the secondary stars in CVs by the emission regions around the white dwarf and the bright spot has been shown to influence the measured K_R (e.g. Wade & Horne 1988; Watson & Dhillon 2001). For example, if absorption lines are quenched on the irradiated side of the secondary, the centre of light will be shifted towards the back of the star. The measured K_R will then be larger than the true (dynamical) value.

Diaz & Hubeny (1999) found evidence for irradiation of the secondary star in V347 Pup, leading them to apply a correction to their measured K_R value. This fact, and the presence of Balmer and He I emission from the inner face of the secondary star seen in the Doppler maps and trailed spectra (Section 3.4), prompted us to look for similar irradiation effects in the absorption lines of our data. We applied the following two observational tests. First, the rotationally broadened line profile would be distorted if there was a non-uniform absorption distribution across the surface of the secondary star (Davey & Smith 1992). This would result in a non-sinusoidal radial velocity curve. Second, one would expect a depletion of secondary-star absorption-line flux at phase 0.5, where the quenched inner hemisphere is pointed towards the observer (e.g. Friend et al. 1990).

The secondary-star radial velocity curves were produced by cross-correlating the V347 Pup spectra with the best-fitting smeared and broadened template spectra, as described in Section 3.6. The cross-correlation peaks were plotted against phase to produce the radial velocity curves shown in the lower panel of Fig. 10. There is evidence for an eccentricity in the radial velocity curve compared with the sinusoidal fit represented by the thin solid line, although the data are noisy.

The variation of secondary-star absorption-line flux with phase for V347 Pup is shown in the top panel of Fig. 10. These light curves were produced by optimally subtracting the smeared and rotationally broadened best-fitting template from the individual CV spectra (with the secondary radial velocity shifted out) as described in Section 3.7. This time, however, the spectra were continuum subtracted rather than normalized to ensure that the measurements were not affected by a fluctuating disc brightness. The constants produced by the optimal subtraction are secondary-star absorption-line fluxes, correct relative to each other, but not in an absolute sense. The dashed lines superimposed on the light curves represent the variation of flux with phase for a Roche lobe with a uniform absorption distribution. The sinusoidal nature is the result of the changing projected area of the Roche lobe through the orbit. The V347 Pup light curve is clearly not represented by a uniform Roche lobe distribution as the secondary-star absorption-line flux vanishes between phases 0.4 and 0.6.

These three pieces of evidence, as well as the disappearance of the CCFs between phases 0.4 and 0.6 seen in Fig. 7, suggest that the secondary star in V347 Pup is irradiated and we must correct the K_R values accordingly.

It is possible to correct K_R for the effects of irradiation by modelling the secondary-star flux distribution. In our simple model, we divided the secondary Roche lobe into 40 vertical slices of equal width from the L_1 point to the back of the star. We then produced a series of model light curves (using the system parameters derived in Section 3.10), varying the numbers of slices omitted from the inner hemisphere of the secondary which contribute to the total flux. The model light curves were then scaled to match the observed data, and the best-fitting model found by measuring the χ^2 between the two. In all models, we used a gravity-darkening parameter $\beta = 0.08$ and

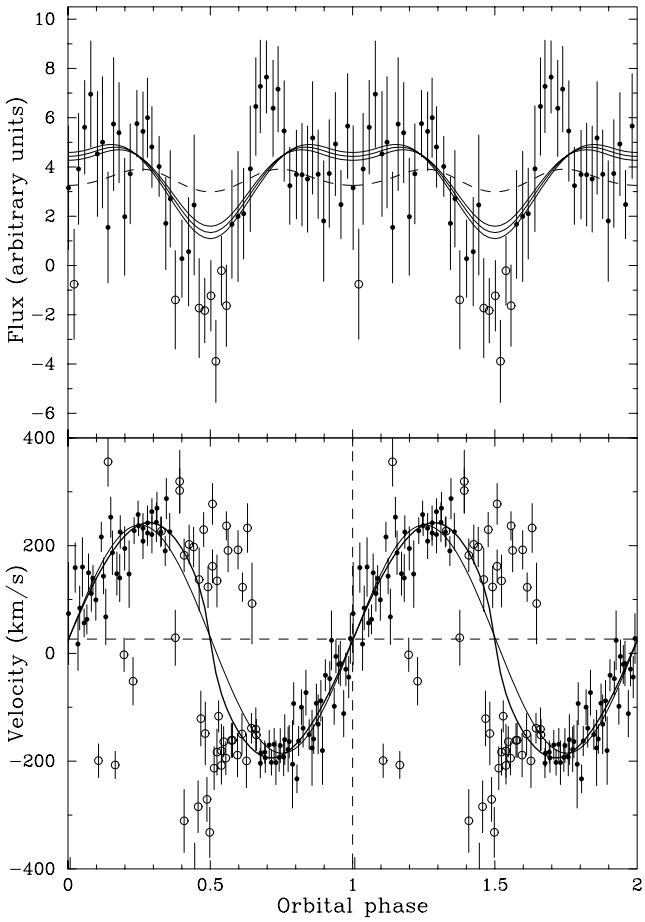

Figure 10. Upper panel: secondary-star absorption line light curve with model fits (solid lines). Model fits are shown for Roche lobes with 11, 12 and 13 slices removed (see text for details). The lower the line, the more slices removed. The dashed line represents a model where no slices have been removed. The data have been phase-binned into 50 bins to increase S/N. Lower panel: measured secondary-star radial velocity curve with a sinusoidal fit (thin solid line) and the best-fitting model fit (thick solid line). In both panels, the open circles indicate points that have been omitted from the fits and the data have been folded to show two orbital phases.

limb-darkening coefficient $u = 0.5$ (e.g. Watson & Dhillon 2001). The negative data points around phase 0.5 were set to zero, as the secondary-star absorption line flux disappears at this point. Once the best-fitting light curve was found, we produced fake V347 Pup spectra from the model, which were cross-correlated with a fake template star to produce a synthetic radial velocity curve. In the first instance, the synthetic curve mimicked the non-sinusoidal nature of the observed data, but with a larger semi-amplitude. This was expected, as the model input parameters used the uncorrected K_R derived in Section 3.10. We then lowered K_R and repeated the process, until the semi-amplitude of the model and observed radial velocity curves were in agreement, each time checking the light-curve models for goodness of fit. The resulting K_R was then adopted as the real (or dynamical) K_R value.

The best-fitting model light curve was produced by omitting 12 slices when fitting the data (reduced χ^2 between model and data $= 1.03$). The model light curves omitting 11, 12 and 13 slices are shown by the solid lines in Fig. 10. Our final model, which has an input K_R of 198 km s^{-1}, produces the radial velocity curve shown as the thick solid line in the lower panel of Fig. 10. There is good

agreement between this and the observed data. If gravity-darkening and limb-darkening are neglected, the best-fitting light curve remains the same, but produce a K_R value which is $\sim$6 km s^{-1} lower.

In summary, we correct the K_R of V347 Pup from 216 km s^{-1} to 198 km s^{-1}. This correction of 18 km s^{-1} is exactly the same as that calculated by Diaz & Hubeny (1999) using a much simpler approximation, which changed their measured value of 205 km s^{-1} to 187 km s^{-1}.

3.9 The distance to V347 Pup

By finding the apparent magnitude of the secondary star from its contribution to the total light of the system, and estimating its absolute magnitude, we can calculate the distance (d) using the equation:

$$5\log(d/10) = m_V - M_V - A_V \quad (4)$$

where A_V is the visual interstellar extinction in magnitudes per kpc.

The mean R-band photometric flux of V347 Pup during the recorded spectra is 8.93 mJy, which we convert to a mean R-band magnitude of 13.8 $\pm$ 0.3. The uncertainty reflects the change in brightness of the system between December 25 and 27. During this time, the secondary star contributes 13 $\pm$ 2 per cent of the total light of the system, assuming an early M spectral type (see Table 4). The apparent magnitude of the secondary is therefore $R = 16.0 \pm 0.4$, which we convert to a V-band magnitude of 17.3 $\pm$ 0.4 using a typical $V - R$ value for an early M star from Gray (1992). There are a number of ways of estimating the absolute magnitude of the secondary star, assuming it is on the main sequence (e.g. Patterson 1984; Gray 1992; Warner 1995b). We took each of these into account and adopted an average value of $M_V = +8.8 \pm 0.5$. Mauche et al. (1994) estimated the extinction to V347 Pup to be $E(B-V) = 0.05$, which results in $A_V = 0.16$ (Scheffler 1982). The distance to V347 Pup is calculated from equation (4) to be 470 $\pm$ 130 pc.

Buckley et al. (1990) estimate the distance to V347 Pup to be between 174 and 380 pc, based on their measured system inclination and out-of-eclipse magnitude. Mauche et al. (1994) use their interstellar reddening measurement and a mean interstellar hydrogen number density to estimate a distance of 340–590 pc. Finally, Diaz & Hubeny (1999) find a distance of 510 $\pm$ 160 pc from the spectral line depths of the secondary star. Our value is consistent with all distance estimates in the literature.

3.10 System parameters

Using the K_R and $v \sin i$ values found in Sections 3.7 and 3.8 in conjunction with the period determined in Section 3.1 and a measurement of the eclipse full-width at half-depth ($\Delta\phi_{1/2}$), we can calculate accurate system parameters for V347 Pup.

In order to determine $\Delta\phi_{1/2}$, we estimated the flux out of eclipse (the principal source of error) and at eclipse minimum, and then measured the full-width of the eclipse half-way between these points. The eclipse full-width at half-depth was measured to be $\Delta\phi_{1/2} = 0.115 \pm 0.005$, in agreement with the eclipse half-width at half-depth of 0.052 ± 0.002 measured by Buckley et al. (1990) at the 2σ level.

We have opted for a Monte Carlo approach similar to Horne, Welsh & Wade (1993) to calculate the system parameters and their errors. For a given set of K_R, $v \sin i$, $\Delta\phi_{1/2}$ and P, the other system parameters are calculated as follows.

R_2/a can be estimated because we know that the secondary star fills its Roche lobe (as there is an accretion disc present and hence mass transfer). R_2 is the equatorial radius of the secondary star and a is the binary separation. We used Eggleton's formula (Eggleton 1983) which gives the volume-equivalent radius of the Roche lobe to better than 1 per cent, which is close to the equatorial radius of the secondary star as seen during eclipse,

$$\frac{R_2}{a} = \frac{0.49q^{2/3}}{0.6q^{2/3} + \ln(1+q^{1/3})}. \quad (5)$$

The secondary star rotates synchronously with the orbital motion, so we can combine K_R and $v \sin i$, to get

$$\frac{R_2}{a}(1+q) = \frac{v \sin i}{K_R}. \quad (6)$$

By considering the geometry of a point eclipse by a spherical body (e.g. Dhillon et al. 1991), the radius of the secondary can be shown to be

$$\left(\frac{R_2}{a}\right)^2 = \sin^2 \pi\Delta\phi_{1/2} + \cos^2 \pi\Delta\phi_{1/2} \cos^2 i, \quad (7)$$

which, using the value of R_2/a obtained using equations (5) and (6), allows us to calculate the inclination, i, of the system. The geometry of a disc eclipse can be approximated to a point eclipse if the light distribution around the white dwarf is axisymmetric (e.g. Dhillon 1990). This approximation is justified given the symmetry of the primary eclipses in the photometry light curves (Fig. 2). Kepler's third law gives us

$$\frac{K_R^3 P_{orb}}{2\pi G} = \frac{M_1 \sin^3 i}{(1+q)^2}, \quad (8)$$

which, with the values of q and i calculated using equations (5), (6) and (7), gives the mass of the primary star. The mass of the secondary star can then be obtained using

$$M_2 = qM_1. \quad (9)$$

The radius of the secondary star is obtained from the equation

$$\frac{v \sin i}{R_2} = \frac{2\pi \sin i}{P}, \quad (10)$$

(e.g. Warner 1995a) and the separation of the components, a, is calculated from equations (6) and (10) with q and i now known.

The Monte Carlo simulation takes 10 000 values of K_R, $v \sin i$ and $\Delta\phi_{1/2}$ (the error on the period is deemed to be negligible in comparison to the errors on K_R, $v \sin i$ and $\Delta\phi_{1/2}$), treating each as being normally distributed about their measured values with standard deviations equal to the errors on the measurements. We then calculate the masses of the components, the inclination of the system, the radius of the secondary star, and the separation of the components, as outlined above, omitting (K_R, $v \sin i$, $\Delta\phi_{1/2}$) triplets which are inconsistent with $\sin i \leqslant 1$. Each accepted M_1, M_2 pair is then plotted as a point in Fig. 11, and the masses and their errors are computed from the mean and standard deviation of the distribution of these pairs.

We find the component masses of V347 Pup to be $M_1 = 0.63 \pm 0.04$ M$_\odot$ and $M_2 = 0.52 \pm 0.06$ M$_\odot$. The values of all the system parameters deduced from the Monte Carlo computation are listed in Table 5, including K_R-corrected and non-K_R-corrected values for comparison. Note that our derived K_W of 163 $\pm$ 9 km s^{-1} is in remarkable agreement with the K_W values of Still et al. (1998) who measure 156 $\pm$ 10 km s^{-1} using a double-Gaussian convolution of the Balmer lines, and 166 km s^{-1} as the centre of axisymmetric Balmer emission. The white dwarf mass of 0.63 $\pm$ 0.04 M$_\odot$ is consistent with the average value of $\overline{M}_1 = 0.80 \pm 0.22$ M$_\odot$ (for CVs above the period gap) determined by Smith & Dhillon (1998). The empirical relation obtained by Smith & Dhillon (1998) between mass and radius for the secondary stars in CVs predicts that if the

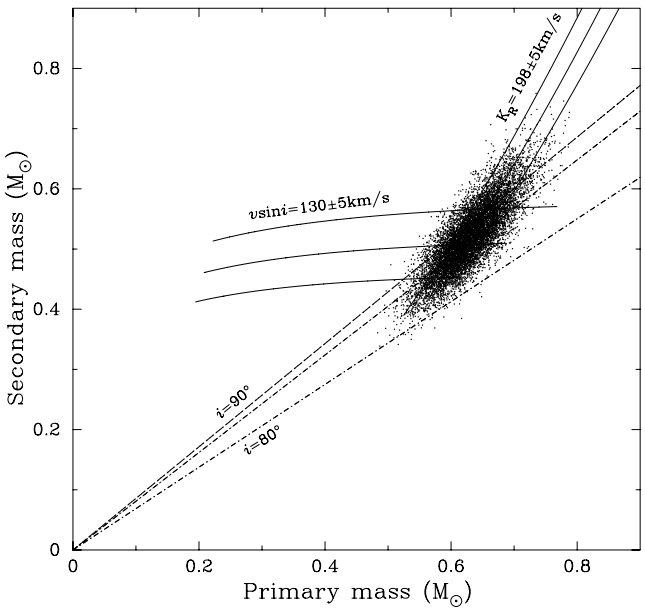

Figure 11. Monte Carlo determination of system parameters for V347 Pup. Each dot represents an M_1, M_2 pair; the solid curves satisfy the $v \sin i$ and K_R constraints, and the dashed lines mark lines of constant inclinations (i = 80°, 85° and 90°).

secondary star in V347 Pup is on the main sequence, it should have a radius of 0.54 ± 0.08 $R_\odot$. Our measured value of 0.60 ± 0.02 $R_\odot$ (from equation 10) is consistent with this value.

4 DISCUSSION

4.1 Spiral arms

Spiral-armed disc asymmetries are evident in the He I and Hβ Doppler maps, confirming the findings of Still et al. (1998) in their Hβ and Hγ maps; see also Papadimitriou et al. (2005) for spiral arms in He I. Similar spiral structures have been observed in dwarf novae during outburst (e.g. IP Peg, Steeghs, Harlaftis & Horne 1997; U Gem, Groot, Rutten & van Paradijs 2001). Tidally driven spiral density waves can develop in accretion discs due to the tidal torque of the mass donor star on the outer disc (Sawada, Matsuda & Hachisu 1986; Blondin 2000; Boffin 2001). Their detection in outburst only reflects the much stronger tidal effects on the accretion disc when it increases in size and temperature during outburst, in which case a tidally induced spiral structure is expected that closely matches the observed structures (Armitage & Murray 1998; Steeghs & Stehle 1999; Steeghs 2001). In dwarf novae, these asymmetries decay as the system returns to quiescence, and the disc cools and shrinks. In order for a similar tidal response to be responsible for the disc asymmetry in V347 Pup, its disc must be large and comparable to the tidal radius. We calculate the tidal radius of the accretion disc to be 0.33a using the pressureless disc models of Paczynski (1977) and our new system parameters. The measured disc radius of R_D/a = 0.28 ± 0.03 is comparable in size to the tidal radius, and therefore consistent with a tidal origin for the observed spiral structure.

Our observations show that the spiral structures are clearly visible in the He I Doppler maps, but are either weak or non-existent in the Balmer and He II maps. This is in contrast to dwarf novae in outburst, which typically show stronger spiral structures in the He II and Balmer lines (e.g. Marsh 2001; Morales-Rueda 2004). This could be a reflection of different densities and temperatures in NL discs compared to the discs of dwarf novae in outburst, or it could simply be due to a contrast effect where the relative contribution of the spiral structure is not as high in the He II and Balmer maps due to the presence of low-velocity emission.

Note that the impact of such tidally induced spiral arms on the angular momentum transport has not been fully established. If they are associated with hydrodynamical shocks, such as in the simulations of Sawada et al. (1986), their contribution to the angular momentum transport could be very significant. On the other hand, Smak (2001) and Ogilvie (2002) propose that these disc structures may reflect tidally thickened areas in the outer disc as it expands close to its tidal radius. Their enhanced emission is then caused by irradiation from the accreting white dwarf and regions close to it.

The prospect of testing such basic disc physics with observations warrants the study of these disc structures in more detail (see also

Table 5. System parameters for V347 Pup. The Monte Carlo results for corrected and uncorrected K_R values are shown for comparison. The radial velocity of the white dwarf (K_W) has also been calculated from the secondary-star parameters.

Parameter	Non-K_R-corrected		K_R-corrected	
	Measured value	Monte Carlo value	Measured value	Monte Carlo value
P_{orb} (d)	0.231 936 060		0.231 936 060	
K_R (km s^{-1})	216 ± 5	215 ± 5	198 ± 5	198 ± 5
$v \sin i$ (km s^{-1})	130 ± 5	131 ± 5	130 ± 5	131 ± 5
$\Delta\phi_{1/2}$	0.115 ± 0.005	0.111 ± 0.003	0.115 ± 0.005	0.113 ± 0.004
q		0.73 ± 0.05		0.83 ± 0.05
i°		85.0 ± 2.1		84.0 ± 2.3
K_W (km s^{-1})		158 ± 9		163 ± 9
M_1($M_\odot$)		0.73 ± 0.05		0.63 ± 0.04
M_2($M_\odot$)		0.54 ± 0.06		0.52 ± 0.06
R_2($R_\odot$)		0.60 ± 0.02		0.60 ± 0.02
a($R_\odot$)		1.72 ± 0.04		1.66 ± 0.05
d (pc)	470 ± 130		470 ± 130	
Spectral type of secondary	M0.5 V		M0.5 V	
$\Delta\phi$	0.110 ± 0.005		0.110 ± 0.005	
R_D/R_1		0.72 ± 0.08		0.72 ± 0.09

Morales-Rueda 2004). With V347 Pup, we have a target that appears to have a persistent disc asymmetry that is more accessible than the transient spiral structures observed in dwarf novae.

4.2 Mass transfer stability

The mass ratio of a CV is of great significance, as it governs the properties of mass transfer from the secondary to the white dwarf primary. This in turn governs the evolution and behaviour of the system.

The secondary star responds to mass loss on two time-scales. First, the star returns to hydrostatic equilibrium on the dynamical time-scale, which is the sound-crossing time of the region affected. Secondly, the star settles into a new thermal equilibrium configuration on a thermal time-scale.

The two time-scales upon which the secondary responds to mass loss leads to two types of mass transfer instability. If, upon mass loss, the dynamical response of the secondary is to expand relative to the Roche lobe, mass transfer is dynamically unstable and mass transfer proceeds on the dynamical time-scale. Politano (1996) made an analytic fit to the models of Hjellming (1989) to give the limit of dynamically stable mass loss, plotted as the solid line in Fig. 12. Dynamically stable mass transfer can occur if the CV lies below this line. This limit is important for low-mass secondary stars ($M_2 < 0.5\ \mathrm{M}_\odot$), as they have significant convective envelopes that tend to expand adiabatically in response to mass loss (de Kool 1992).

Thermally unstable mass transfer is possible if the dynamic response of the star to mass loss is to shrink relative to its Roche lobe (i.e. mass transfer is *dynamically* stable). This occurs at high donor masses ($M_2 > 0.8\ \mathrm{M}_\odot$) when the star has a negligible convective envelope and its adiabatic response to mass loss is to shrink. (e.g. de Kool 1992; Politano 1996). Mass transfer then initially breaks contact and the star begins to settle into its new thermal equilibrium configuration. If the thermal equilibrium radius of the star is now bigger than the Roche lobe, mass transfer is again unstable, but proceeds on the slower, thermal time-scale. The limit of thermally stable mass transfer can be found by differentiating the main-sequence mass–radius relationship given in Politano (1996). Thermally stable mass transfer can occur if the CV appears below the dotted line plotted in Fig. 12.

The limit for dynamically stable mass transfer is important in the case of V347 Pup owing to the low secondary-star mass. Fig. 12 shows that the system is just consistent with the limit at the 1σ level. The mass transfer stability limits, however, are true only for zero-age main sequence (ZAMS) stars, whereas the secondary stars in CVs are expected to have undergone some evolution. The loss of the outer envelope, for example, would result in a larger than normal helium-to-hydrogen ratio and affect the response of the star to mass loss. For instance, DX And, which lies outside the limit, has been shown to have an evolved companion (Drew, Jones & Woods 1993).

There is tentative evidence that the secondary star in V347 Pup is evolved by considering three pieces of evidence. First, V347 Pup falls outside the limit for dynamically stable mass transfer (although agrees at the 1σ level). Secondly, the measured radius is at the upper limit for a main-sequence companion of the same mass (Smith & Dhillon 1998). Third, the secondary-star mass and spectral type measured for V347 Pup are closer to the evolved models of Kolb et al. (2001) than the ZAMS models.

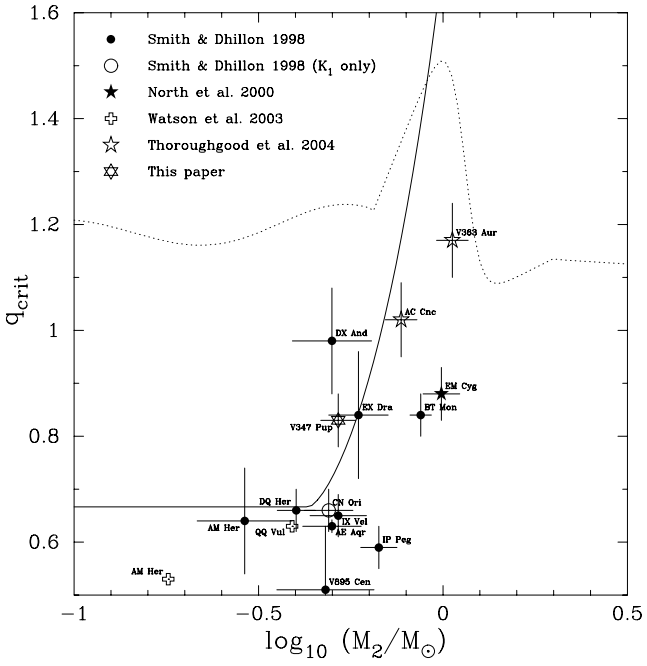

Figure 12. Critical mass ratios for mass transfer stability. The dotted line represents the condition for thermal instability; the solid line represents the condition for dynamical instability (Politano 1996). Both curves assume the star is initially in thermal equilibrium. Mass ratios and secondary masses from the compilation of Smith & Dhillon (1998), North et al. (2000), Watson et al. (2003) and Thoroughgood et al. (2004) are overplotted. The mass ratios and secondary-star masses of V347 Pup determined in this paper are also plotted.

5 CONCLUSIONS

(i) We have measured the radial and rotational velocities of the secondary star in V347 Pup in order to calculate the component masses and other system parameters. The secondary-star radial velocity is affected by irradiation from the emission regions around the primary, which we correct for using a model. We find the component masses in V347 Pup to be $M_1 = 0.63 \pm 0.04\ \mathrm{M}_\odot$ for the white dwarf primary and $M_2 = 0.52 \pm 0.06\ \mathrm{M}_\odot$ for the M0.5V secondary star. V347 Pup shows many of the characteristics of the SW Sex stars, exhibiting single-peaked emission lines, high-velocity S-wave components and phase-offsets in the radial velocity curves.

(ii) V347 Pup lies outside the theoretical limit for dynamically stable mass transfer in ZAMS stars, but is just consistent at the 1σ uncertainty level. This piece of evidence, together with a secondary-star radius at the upper limit for a main-sequence companion of the same mass, suggests that the secondary star in V347 Pup may be evolved. Additionally, the secondary-star mass and spectral type measured for V347 Pup are closer to the evolved models of Kolb et al. (2001) than the ZAMS models.

(iii) The presence of spiral arms in the accretion disc, first noted by Still et al. (1998), has been confirmed. Consistent with this, we find that the measured accretion disc radius is close to the tidal radius computed from the pressureless disc models of Paczynski (1977). The persistent spiral arms seen in this bright nova-like makes it an excellent candidate in which to study these features, rather than the transient spiral structures observed in dwarf novae.

ACKNOWLEDGMENTS

TDT is supported by a PPARC studentship; CAW is supported by PPARC grant number PPA/G/S/2000/00598; SPL is supported by

PPARC. DS acknowledges a Smithsonian Astrophysical Observatory Clay Fellowship.

REFERENCES

Armitage P. J., Murray J. R., 1998, MNRAS, 297, L81
Baptista R., Cieslinski D., 1991, IAU Circ., 5407
Blondin J. M., 2000, New Astron., 5, 53
Boffin H. M. J., 2001, in Boffin H., Steeghs D., Cuypers J., eds, Proc. Int. Workshop on Astrotomography. Springer-Verlag, Düsseldorf, p. 69
Buckley D. A. H., Sullivan D. J., Remillard R. A., Tuohy I. R., Clark M., 1990, ApJ, 355, 617
Davey S. C., Smith R. C., 1992, MNRAS, 257, 476
de Kool M., 1992, A&A, 261, 188
Dhillon V. S., 1990, DPhil. thesis, Univ. Sussex
Dhillon V. S., Marsh T. R., Jones D. H. P., 1991, MNRAS, 252, 342
Dhillon V. S., Marsh T. R., Jones D. H. P., Smith R. C., 1992, MNRAS, 258, 225
Dhillon V. S., Jones D. H. P., Marsh T. R., 1994, MNRAS, 266, 859
Dhillon V. S., Marsh T. R., Jones D. H. P., 1997, MNRAS, 291, 694
Diaz M. P., Hubeny I., 1999, ApJ, 523, 786
Drew J. E., Jones D. H. P., Woods J. A., 1993, MNRAS, 260, 803
Eggleton P. P., 1983, ApJ, 268, 368
Friend M. T., Martin J. S., Smith R. C., Jones D. H. P., 1990, MNRAS, 246, 637
Gray D. F., 1992, The Observation and Analysis of Stellar Photospheres. Cambridge Univ. Press, Cambridge
Groot P. J., Rutten R. G. M., van Paradijs J., 2001, A&A, 368, 183
Harrop-Allin M. K., Warner B., 1996, MNRAS, 279, 219
Hjellming M. S., 1989, PhD thesis, Univ. Illinois
Honeycutt R. K., 2001, PASP, 113, 473
Horne K., Marsh T. R., 1986, MNRAS, 218, 761
Horne K., Welsh W. F., Wade R. A., 1993, ApJ, 410, 357
Knigge C., Long K. S., Hoard D. W., Szkody P., Dhillon V. S., 2000, ApJ, 539, L49
Kolb U., King A. R., Baraffe I., 2001, MNRAS, 321, 544
Marsh T. R., 1988, MNRAS, 231, 1117
Marsh T. R., 2001, in Boffin H., Steeghs D., Cuypers J., eds, Proc. Int. Workshop on Astrotomography. Springer-Verlag, Düsseldorf, p. 1
Marsh T. R., Horne K., 1988, MNRAS, 235, 269
Mason E., Howell S. B., 2003, A&A, 403, 699
Mauche C. W., Raymond J. C., Buckley D. A. H., Mouchet M., Bonnell J., Sullivan D. J., Bonnet-Bidaud J., Bunk W. H., 1994, ApJ, 424, 347
Morales-Rueda L., 2004, Astron. Nachr., 325, 193
North R. C., Marsh T. R., Moran C. K. J., Kolb U., Smith R. C., Stehle R., 2000, MNRAS, 313, 383
Ogilvie G. I., 2002, MNRAS, 330, 937
Paczynski B., 1977, ApJ, 216, 822
Papadimitriou C. J., Harlaftis E. T., Steeghs D., Niarchos P. G., 2005, in Hameury J. M., Lasota J.-P., eds, ASP Conf. Ser. Vol. 330, The Astrophysics of Cataclysmic Variables and Related Objects. Astron. Soc. Pac., San Francisco, in press
Patterson J., 1984, ApJS, 54, 443
Politano M., 1996, ApJ, 465, 338
Rappaport S., Verbunt F., Joss P. C., 1983, ApJ, 275, 713
Sawada K., Matsuda T., Hachisu I., 1986, MNRAS, 219, 75
Scheffler H., in Schaifers K., Voigt H. H., eds, Landolt–Börnstein Numerical Data and Functional Relationships in Science and Technology, New Series, Group VI, Vol. 2c. Springer Verlag, Heidelberg, p. 47
Schneider D. P., Young P. J., 1980, ApJ, 238, 946
Shafter A. W., Szkody P., Thorstensen J. R., 1986, ApJ, 308, 765
Shafter A. W., Hessman F. V., Zhang E. H., 1988, ApJ, 327, 248
Shlosman I., Vitello P., Mauche C. W., 1996, ApJ, 461, 377
Skilling J., Bryan R. K., 1984, MNRAS, 211, 111
Smak J. I., 2001, Acta Astron., 51, 295
Smith D. A., Dhillon V. S., 1998, MNRAS, 301, 767
Smith D. A., Dhillon V. S., Marsh T. R., 1998, MNRAS, 296, 465
Spruit H. C., Ritter H., 1983, A&A, 124, 267
Steeghs D., 2001, in Boffin H., Steeghs D., Cuypers J., eds, Proc. Int. Workshop on Astrotomography. Springer-Verlag, Dusseldorf, p. 45
Steeghs D., 2003, MNRAS, 344, 448
Steeghs D., Stehle R., 1999, MNRAS, 307, 99
Steeghs D., Harlaftis E. T., Horne K., 1997, MNRAS, 290, L28
Still M. D., Dhillon V. S., Jones D. H. P., 1995, MNRAS, 273, 863
Still M. D., Buckley D. A. H., Garlick M. A., 1998, MNRAS, 299, 545
Thoroughgood T. D., Dhillon V. S., Littlefair S. P., Marsh T. R., Smith D. A., 2001, MNRAS, 327, 1323
Thoroughgood T. D., Dhillon V. S., Watson C. A., Buckley D. A. H., Steeghs D., Stevenson M. J., 2004, MNRAS, 353, 1135
Vande Putte D., Smith R. C., Hawkins N. A., Martin J. S., 2003, MNRAS, 342, 151
Wade R. A., Horne K., 1988, ApJ, 324, 411
Warner B., 1995a, Cataclysmic Variable Stars. Cambridge Univ. Press, Cambridge
Warner B., 1995b, Ap&SS, 232, 89
Watson C. A., Dhillon V. S., 2001, MNRAS, 326, 67
Watson C. A., Dhillon V. S., Rutten R. G. M., Schwope A. D., 2003, MNRAS, 341, 129

This paper has been typeset from a TEX/LATEX file prepared by the author.